Temperature distributions in the laser-heated diamond anvil cell from 3-D numerical modeling

E. S. G. Rainey, J. W. Hernlund, and A. Kavner

Citation: J. Appl. Phys. **114**, 204905 (2013); doi: 10.1063/1.4830274
View online: http://dx.doi.org/10.1063/1.4830274
View Table of Contents: http://aip.scitation.org/toc/jap/114/20
Published by the American Institute of Physics

Temperature distributions in the laser-heated diamond anvil cell from 3-D numerical modeling

E. S. G. Rainey,[1] J. W. Hernlund,[2,3] and A. Kavner[1]
[1]*Department of Earth and Space Sciences, University of California, Los Angeles, California 90095, USA*
[2]*Department of Earth and Planetary Science, University of California, Berkeley, California 94720, USA*
[3]*Earth-Life Science Institute, Megoro, Tokyo 152-8551, Japan*

(Received 21 July 2013; accepted 30 October 2013; published online 27 November 2013)

We present TempDAC, a 3-D numerical model for calculating the steady-state temperature distribution for continuous wave laser-heated experiments in the diamond anvil cell. TempDAC solves the steady heat conduction equation in three dimensions over the sample chamber, gasket, and diamond anvils and includes material-, temperature-, and direction-dependent thermal conductivity, while allowing for flexible sample geometries, laser beam intensity profile, and laser absorption properties. The model has been validated against an axisymmetric analytic solution for the temperature distribution within a laser-heated sample. Example calculations illustrate the importance of considering heat flow in three dimensions for the laser-heated diamond anvil cell. In particular, we show that a "flat top" input laser beam profile does not lead to a more uniform temperature distribution or flatter temperature gradients than a wide Gaussian laser beam. © *2013 AIP Publishing LLC*. [http://dx.doi.org/10.1063/1.4830274]

I. INTRODUCTION

The laser-heated diamond anvil cell (LHDAC) is the experimental tool for reaching static high pressures and temperatures that correspond to the conditions of the deep interiors of terrestrial planets and moons. The diamond anvil cell is capable of subjecting materials to over 300 GPa of pressure, and materials can be heated to thousands of degrees by focusing infrared lasers onto the sample through the transparent diamond anvils [e.g., Ref. 1]. *In situ* characterization of sample properties can be performed using microscopy, spectroscopy, and a variety of X-ray-based tools including scattering and diffraction. Interpreting the data in terms of deep Earth and planetary interior applications requires both accuracy and precision in the measurements of properties, pressures, and temperatures. Very high temperatures are difficult to generate and control in the diamond anvil cell because of the small sample sizes and the fact that the samples are in close proximity to a relatively much larger volume of high-thermal-conductivity diamond, which behaves effectively as a heat sink. Therefore, a great deal of continuous wave (CW) laser power needs to be absorbed by the sample in order to maintain quasi-steady-state hotspot temperatures. Most mineral physics LHDAC experiments involve this type of continuous heating. Because of the extreme heat flow conditions, the steady-state temperature gradients in both the axial and radial directions are steep, and the temperature distribution is difficult to measure accurately, leading to absolute uncertainties and misleading error analysis for measurements of physical properties including phase stability, melting temperatures, equations of state, and chemical partitioning at high pressures and temperatures in the LHDAC.

Mathematical models of LHDAC temperature gradients are useful for multiple purposes. These include estimating the magnitude of temperature gradients for a particular experimental design, calculating the effect of temperature gradients on real measurements,[2] creating synthetic temperature vs. power curves for thermal conductivity measurements,[3,4] and estimating uncertainties in measured temperatures arising from uncertainties in experimental properties. For example, one of the important applications of the LHDAC is its use in conjunction with synchrotron-based X-ray diffraction to measure material phase and lattice volume *in situ* at high pressures and temperatures. For high-quality powder X-ray diffraction measurements, the sample volume should be maximized. But during laser heating, especially at high pressures, this can possibly be compromised by large temperature gradients over the X-rayed volume. The three-dimensional nature of the temperature gradients means that if there are temperature gradients present over the length scale of the X-ray spot, the X-ray volume will be heavily biased towards the lower temperatures within the X-ray volume, even if the hotspot is well-centered.[2] Multiple approaches should be taken to fully address this issue, including considerations in experimental design, such as broadening the laser hotspot, as well as in data analysis, such as providing a precise measurement of the temperature gradient and the relationship between the hotspot and the X-ray beam during laser heating. Modeled 3-D temperature gradients can be used to aid in experimental design as well as to quantify the effect of temperature gradients on the experimental results. Similar methods have also been used in other kinds of high-pressure experiments to improve designs and minimize thermal gradients.[5]

We created a 3-D numerical code (TempDAC) for modeling heat flow within the LHDAC that allows us to calculate the steady-state temperature distribution during continuous heating experiments. Here, we present and discuss the model, validate it against an existing lower-dimensional analytical model, and use it to demonstrate various trends for temperature distributions in the diamond anvil cell. Like existing

models,[3,6–9] TempDAC solves the steady-state heat conduction equation within the LHDAC. However, previous numerical and analytic LHDAC models presented in the literature have assumed either axisymmetry and/or temperature-independent thermal conductivity. The TempDAC model is a fully 3-D model with flexible geometries, allowing it to be tailored to model particular experimental conditions. The sample can be modeled as a single partially absorbing material with a specified laser absorption coefficient, or as a composite, e.g., a transparent insulator with an opaque metal foil of specified thickness. Thermal conductivities are material-, temperature-, and can be direction-dependent (i.e., anisotropic). Laser heating can be modeled as single- or double-sided, with a customizable beam profile. The 3-D nature and flexible geometries of TempDAC allow it to fully describe the three dimensional temperature distributions that are inherent in CW LHDAC experiments.

II. MODEL DESCRIPTION

A. LHDAC thermal environment

The characteristics of LHDAC temperature distributions are governed by the high thermal mass of the diamond anvils compared with the sample and the small physical size of the experiments. These factors result in steep temperature gradients in the axial and radial directions as well as fast timescales for thermal equilibration. For example, for a typical sample thickness L of a few tens of microns and a thermal diffusivity κ of $\sim 10^{-6}$ m^2/s, the heat diffusion timescale (L^2/κ) across the sample is $\sim 10^{-4}$ s. Across $\sim$3-mm diamond anvils, it is $\sim 10^{-2}$ s (assuming $\kappa \sim 10^{-3}$ m^2/s for diamond). Thus, during heating with CW laser power, steady-state temperature distributions emerge very quickly and decay quickly once the laser is turned off. During CW laser heating, the typical temperature gradients within the sample chamber are extreme (on the order of 100 K/μm, see example in Fig. 3). Although samples within the diamond cell do radiate some energy away (indeed, the typical method of temperature measurement in LHDAC experiments is spectroradiometry), the extreme temperature gradients mean that lattice conduction is expected to be the dominant mechanism of heat transport within the diamond cell in most experiments, and measured temperature gradients are consistent with heat transport by phonons.[8–11] The steady-state heat conduction equation has been shown to be appropriate to describe heat flow within the LHDAC for continuous heating experiments and has been used in previous models [e.g., Refs. 8 and 9]. An ambient temperature boundary condition is expected to be valid due to the small sample size and high thermal conductivity of the diamond anvils and metal gasket. However, in real laser heating experiments, the diamond anvil cell does not remain in steady state; in fact, the entire cell slowly warms over the course of a heating experiment. Typically, the temperature change is at most a few tens of degrees, such that the approximation of a steady state with ambient temperature boundaries remains valid, especially for short experiments or lower peak temperatures. At synchrotron facilities, diamond cells are often water-cooled to maintain the cell at a constant temperature during laser heating.

B. Governing equations and numerical implementation

The TempDAC model builds upon a previous thermal modeling effort[12] for describing temperature distributions within solid-medium high-pressure experiments, extending the solution to the full 3-D case. As in the previous model, the equation governing heat conduction within the LHDAC is written as

$$\nabla \cdot \underline{k} \nabla T + Q = 0, \tag{1}$$

where $\underline{k}$ is the thermal conductivity tensor, T is temperature, and Q is an internal heating term representing the absorbed laser power. If the principal axes of the thermal conductivity tensor are aligned with the Cartesian coordinates x, y, and z, then Eq. (1) becomes

$$\frac{\partial}{\partial x}\left(k_x \frac{\partial T}{\partial x}\right) + \frac{\partial}{\partial y}\left(k_y \frac{\partial T}{\partial y}\right) + \frac{\partial}{\partial z}\left(k_z \frac{\partial T}{\partial z}\right) + Q = 0, \tag{2}$$

where k_x, k_y, and k_z represent the inner products of the thermal conductivity tensor with unit vectors along the x, y, and z axes, respectively.

The numerical model domain is illustrated in Fig. 1. The domain is cubic and comprises equal-sized rectangular cells. The full extent and shape of the diamond anvils and metal

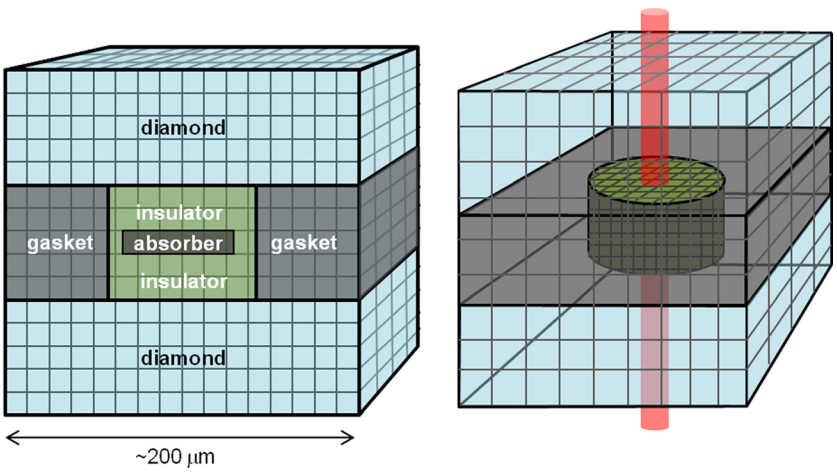

FIG. 1. Illustration of the numerical model domain. The image on the left depicts an axial slice through the domain. The presence of a laser absorber is optional. The image on the right is a view of the interior of the model domain. Note that the sizes of the sample chamber and absorber and the domain length scale are all flexible and not confined to the particular geometry depicted in the cartoon.

gasket are not modeled. But, since the temperature generally drops to ambient values within or very close to the edges of the sample chamber, this is not expected to affect the calculated temperature distribution. For cells with dimensions Δx, Δy, and Δz, a finite volume form of Eq. (2) can be written as

$$\begin{aligned} & k_{x;i+\frac{1}{2},j,k}\frac{T_{i+1,j,k}-T_{i,j,k}}{\Delta x^2}+k_{x;i-\frac{1}{2},j,k}\frac{T_{i-1,j,k}-T_{i,j,k}}{\Delta x^2} \\ & +k_{y;i,j+\frac{1}{2},k}\frac{T_{i,j+1,k}-T_{i,j,k}}{\Delta y^2}+k_{y;i,j-\frac{1}{2},k}\frac{T_{i,j-1,k}-T_{i,j,k}}{\Delta y^2} \\ & +k_{z;i,j,k+\frac{1}{2}}\frac{T_{i,j,k+1}-T_{i,j,k}}{\Delta z^2}+k_{z;i,j,k-\frac{1}{2}}\frac{T_{i,j,k-1}-T_{i,j,k}}{\Delta z^2} \\ & +Q_{i,j,k}=0. \end{aligned} \tag{3}$$

The subscripts i, j, and k are used to refer to the value of a parameter at a particular discrete cell (e.g., $T(i\Delta x, j\Delta y, k\Delta z) \rightarrow T_{i,j,k}$). The temperatures are defined at the center of each cell, while the conductivities are defined on the faces (displaced $1/2$ cell length from the cell centers). Each cell consists of a single material (e.g., diamond, gasket, sample) and has its own functional variation of thermal conductivity with temperature. Therefore, thermal conductivity is naturally defined at the center of each cell and interpolation is required to obtain thermal conductivity values at the cell faces, which is most compatible with the calculation of heat flux at the midpoint between adjacent cells. In our implementation, the harmonic interpolant is used, since it is the only interpolation that exactly conserves the continuity of heat flux between cells. The conductivity values in Eq. (3) are obtained from the cell-center conductivity values using the formulas

$$\begin{aligned} k_{x;i-\frac{1}{2},j,k} &= \frac{2k_{x;i,j,k}k_{x;i-1,j,k}}{k_{x;i,j,k}+k_{x;i-1,j,k}}, & k_{x;i+\frac{1}{2},j,k} &= \frac{2k_{x;i,j,k}k_{x;i+1,j,k}}{k_{x;i,j,k}+k_{x;i+1,j,k}}, \\ k_{y;i,j-\frac{1}{2},k} &= \frac{2k_{y;i,j,k}k_{y;i,j-1,k}}{k_{y;i,j,k}+k_{y;i,j-1,k}}, & k_{y;i,j+\frac{1}{2},k} &= \frac{2k_{y;i,j,k}k_{y;i,j+1,k}}{k_{y;i,j,k}+k_{y;i,j+1,k}} \\ k_{z;i,j,k-\frac{1}{2},} &= \frac{2k_{z;i,j,k}k_{z;i,j,k-1}}{k_{z;i,j,k}+k_{z;i,j,k-1}}, & k_{z;i,j,k+\frac{1}{2},} &= \frac{2k_{z;i,j,k}k_{z;i,j,k+1}}{k_{z;i,j,k}+k_{z;i,j,k+1}}. \end{aligned} \tag{4}$$

When boundary conditions are imposed, Eq. (3) becomes an invertible system of equations over the entire model domain. We choose to apply the condition that the exterior boundaries of the domain remain at a constant temperature T_c, where T_c is some ambient temperature (typically 300 K). The boundary condition is enforced using ghost cells adjacent to and outside of the edges of the domain. The ghost cells are the same size as the interior cells and are considered to have the same thermal conductivity as their immediate neighbor cells.

The absorbed laser power is modeled in one of two ways, depending on whether the sample is assumed to consist of (1) an opaque absorbing foil within a transparent insulating material, or (2) a partially absorbing material. For an opaque foil, the heating term $Q_{i,j,k}$ is assumed to be nonzero only within cells at the foil surface where the laser is incident, i.e., the laser is assumed to be absorbed only at the edge of the foil. If the laser is aligned with the z-direction, then $Q_{i,j,k}$ varies with x and y according to the assumed 2-D intensity distribution of the laser beam. For the case of a partially absorbing material, $Q_{i,j,k}$ is nonzero within the entire sample and varies with x and y according to the laser beam intensity distribution and with z depending on the assumed material absorption coefficient. In this case, $Q_{i,j,k}$ is written as

$$Q_{i,j,k} = \alpha I_{i,j,k-1}, \tag{5}$$

where α is the absorption coefficient of the material and $I_{i,j,k-1}$ is the laser intensity passing from cell $(i,j,k-1)$ into cell (i,j,k). Integrating Eq. (5) over a sample of thickness L gives the Beer's law result that the total absorbed power is equal to $P_l(1-\exp(\alpha L))$, where P_l is the total laser power. Therefore, partially absorbing samples are conveniently described by an optical thickness τ that is the product of the absorption coefficient and the sample thickness: $\tau = \alpha L$.

C. Solution method

The numerical implementation uses a full approximation storage multi-grid solver. This technique allows for high resolution near the center of the sample where temperature gradients are very large while leaving other areas of the domain less resolved in order to save computation time. The linear system can be written as

$$L^h T^h = F^h, \tag{6}$$

where $F^h = -Q^h$ on the finest grid. Let, $\check{T}^h$ be a guess or approximation of T^h, and define the error as $e^h = T^h - \check{T}^h$. Then, Eq. (6) can be written as

$$L^h e^h = R^h = F^h - L^h \check{T}^h, \tag{7}$$

where R^h is the residual on grid h. The residual is interpolated to a coarser grid H, giving

$$L^H T^H = L^H e^H + L^H\left(I_h^H T^h\right) = I_h^H R^h + L^H\left(I_h^H T^h\right), \tag{8}$$

where the initial guess for T^H is given by $I_{\mathrm{h}}^{\mathrm{H}} T^h$. The full approximation for temperature is thus stored on each grid level in this method, allowing one to treat non-linearity at both coarse and fine scales.

III. VALIDATION OF NUMERICAL SOLUTION

In order to verify the output of the numerical model, we compared it against an analytic solution for the temperature distribution within a laser-heated DAC sample. An analytic solution exists for the simplified case of a cylindrically symmetric sample with temperature-dependent thermal conductivity, as shown by Panero and Jeanloz.[9] In their model, the sample is represented by a cylinder with boundaries at ambient temperature and uniform heating in the axial direction. The analytical model domain is shown in Fig. 2. Although the analytical model domain is not exactly equivalent to the numerical model, which explicitly includes the effects of the diamond anvils and metal gasket, it was shown to closely replicate the temperature profiles from previous numerical simulations.[9] The assumption of ambient-temperature

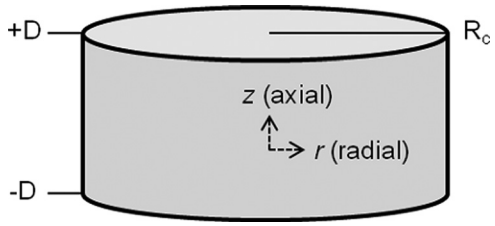

FIG. 2. Illustration of the geometry of the analytical model domain, representing a cylindrically symmetric partially absorbing sample.

boundaries has also been demonstrated to be valid by previous numerical models, which have shown that the temperature within a laser-heated diamond cell drops to near-ambient at the surfaces of the diamond anvils in the axial direction (z, parallel to laser beam) and within the sample chamber in the radial direction (r, perpendicular to laser beam) [e.g., Ref. 6]. The assumption of uniform axial heating is applicable to the case of a partially absorbing sample without insulating layers that is optically thin. The steady-state heat conduction equation for a laser in TEM_{00} mode can then be written as[9]

$$\nabla \cdot (k(T)\nabla T) = -A_0 \exp\left(\frac{r^2}{R^2}\right). \tag{9}$$

Here, k is the thermal conductivity of the sample, T is temperature, A_0 is the peak volumetric absorbed power, r is radius, and R is the Gaussian laser waist size. Panero and Jeanloz[9] linearized this equation using the Kirchhoff transform

$$\theta = \frac{1}{k_0}\int_{T_0}^{T} k(\tau)d\tau, \tag{10}$$

where k_0 is the thermal conductivity at temperature T_0. The heat equation can then be solved analytically for θ and transformed to a solution for T using any assumed temperature dependence of the sample thermal conductivity. Following the analysis of Panero and Jeanloz,[9] the general solution for θ for a cylindrical sample of thickness $2D$ and radius R_c is

$$\theta = \frac{A_0 R^2}{k_0}\left(\frac{1}{4}E_1(R_c^2) - \frac{1}{4}E_1(r^2) + \frac{1}{2}\log\left(\frac{R_c}{r}\right)\right) + \sum\nolimits_i c_i \cosh\left(\frac{a_i D}{R_c R}z\right) J_0\left(\frac{a_i}{R_c}r\right), \tag{11}$$

where E_1 is the exponential integral function, J_0 is the zeroth-order Bessel function of the first kind, a_i is the ith root of J_0, c_i are constants, and z is the axial coordinate which extends from $-D$ to $+D$. The constants c_i are calculated in order to satisfy the boundary conditions. Panero and Jeanloz[9] provided numerical solutions to c_i for a particular experimental geometry. A general form for the constants c_i can be found using the orthogonality of Bessel functions. The solution for c_i is then written as

$$c_i = \frac{-\frac{A_0 R^2}{k_0}\int_0^{R_c}\left(\frac{1}{4}E_1(R_c^2) - \frac{1}{4}E_1(r^2) + \frac{1}{2}\log\left(\frac{R_c}{r}\right)\right)J_0\left(\frac{a_i}{R_c}r\right)rdr}{\int_0^{R_c}\cosh\left(\frac{a_i D}{R_c R}z\right)J_0\left(\frac{a_i}{R_c}r\right)J_0\left(\frac{a_i}{R_c}r\right)rdr}. \tag{12}$$

Temperature profiles calculated using Eqs. (9)–(12) are compared with the output from TempDAC in Fig. 3. The analytic solution was calculated out to $i = 5$ only, since adding further terms resulted in a change in the peak temperature of less than 0.1%. For the comparison, we assumed a sample thickness of 50 μm, sample radius 90 μm, and laser profile full width at half max of 20 μm. The boundary temperature was set to $T_0 = 300$ K. The sample thermal conductivity was chosen to be 4.0 W/m K at ambient temperature T_0, which is the approximate value for iron-bearing olivine.[13] For the numerical model, we used ambient-temperature thermal conductivities of 1000 W/m K for the diamond anvils[14] and 48.0 W/m K for the metal gasket (appropriate for rhenium).[15] A T^{-1} temperature dependence of thermal conductivity was assumed for all materials. To compare the analytic and numerical calculations, the assumed laser power was adjusted such that the peak temperature was calculated to be 2500 K in the analytic solution (0.7812 W for the model parameters used here). This laser power value was then used as an input in TempDAC, which was run at multiple grid resolutions to test the convergence of the numerical solution. The results of this test are in Table I. The solutions for grid sizes $128 \times 128 \times 128$ and $256 \times 256 \times 256$ are nearly identical, and well within the margin of error for LHDAC temperature measurements both compared to each other and to the analytic solution. Note that we would not expect the numerical solution to converge exactly to the analytic one, due to the difference in boundary conditions between the models.

IV. EXAMPLE CALCULATIONS

The TempDAC numerical model can be used to test hypotheses regarding the thermal response of samples heated in the diamond anvil cell, to aid in experimental design, and to help interpret experimental results. In this section, we show numerical results simulating several different types of LHDAC experiments in order to demonstrate the use of our model and to elucidate the characteristics of temperature distributions within LHDAC samples in the context of real and imagined experiments. For reference, the assumed

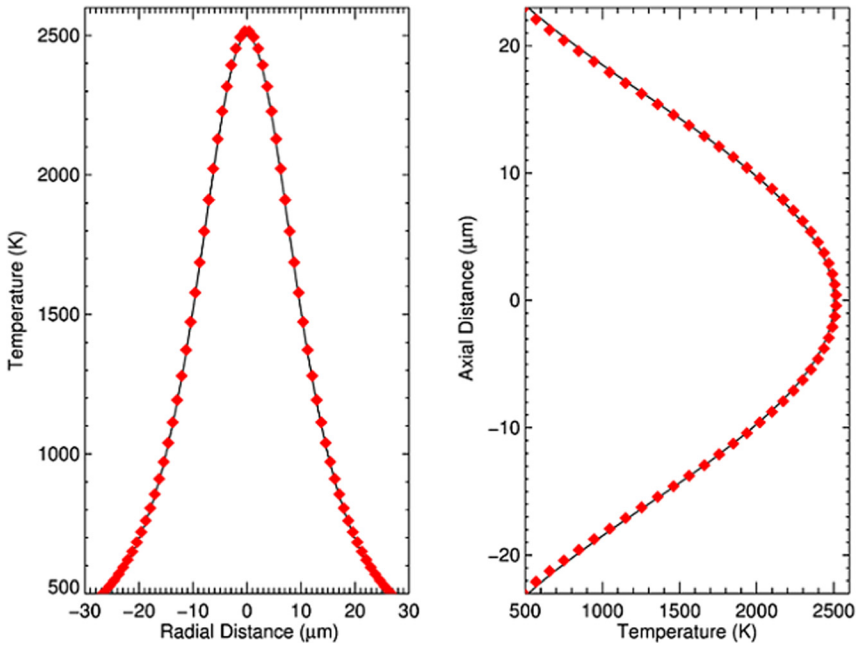

FIG. 3. Comparison of radial (left plot) and axial (right plot) temperature profiles from the analytic model of Eqs. (9)–(12) and the TempDAC numerical solution. Temperatures at the TempDAC grid points are represented by red diamonds; the solid black line represents the analytic solution. The numerical result shown was calculated for grid size $256 \times 256 \times 256$.

properties of the materials used in our example calculations are compiled in Table II.

A. Partially absorbing sample with elliptical laser

In many experimental applications, a laser beam will not necessarily have perfectly circular symmetry about the propagation direction. Because the sample temperature distribution is strongly influenced by the shape of the laser power profile, it is important to model the laser shape as accurately as possible when calculating LHDAC temperature distributions with the goal of interpreting experimental data. We modeled the temperature distribution for an elliptical Gaussian laser heating an isotropic, partially absorbing olivine sample with an optical thickness τ of 1.0, where τ is defined as in Sec. II B, a room-temperature thermal conductivity of 4 W/m K,[13] and a T^{-1} temperature dependence of thermal conductivity. The laser beam was an elliptical Gaussian with a FWHM of 20 μm along the x-axis and 30 μm along the y-axis. The sample thickness was set to 40 μm, and the sample radius 80 μm. A rhenium gasket with a room temperature thermal conductivity of 48 W/m K (Ref. 15) was assumed. Fig. 4 shows the 2D radial temperature distribution at the peak of the temperature profile, near the center of the sample. Although the sample is isotropic, the temperature contours are elliptical due to the influence of the laser beam shape. The temperature contours are slightly less elliptical than the laser beam, owing to the presence of axial as well as radial heat flow within the LHDAC.

Additional models were run for sample optical thicknesses $\tau = 0.5$ and $\tau = 2.0$. For each model, the laser power was tuned to give the same peak sample temperature of 2350 K. Since the peak temperature, sample and laser geometries, and sample thermal conductivity were the same for each model, the radial temperature distributions at the peak temperature are the same. However, the axial temperature distributions differ as shown in Fig. 5. As the optical thickness increases, the peak temperature occurs closer to the heated side, and less laser power is required to heat the sample to the same temperature due to the increased absorption coefficient. For the case of $\tau = 0.5$, a total laser power of 1.8 W was required; the power was $\sim$37% lower for $\tau = 1.0$ and $\sim$53% lower for $\tau = 2.0$.

TABLE I. Peak temperature and RMS error for TempDAC numerical model run with grid size $n \times n \times n$. All models were run using the same absorbed laser power.

n	Fine grid cell size (μm)	Peak temperature (K)	RMS error (K)
16	13.3	876	140.2
32	6.7	1730	78.4
64	3.3	2235	31.8
128	1.7	2515	4.4
256	0.83	2515	4.2
Analytic	—	2500	0.0

TABLE II. List of materials used in the TempDAC model validation and example calculations and the ambient-temperature thermal conductivity of each material. For all materials, the thermal conductivity was assumed to vary inversely with temperature except Pt and MgO, for which the temperature thermal conductivity functions were taken from Terada *et al.*[18] and Tang and Dong,[19] respectively.

Material	Thermal conductivity at 300 K (W/m K)	Source
Diamond	1000	Ref. 14
Rhenium	48.0	Ref. 15
Olivine	4.0	Ref. 13
Graphite	6.8	Ref. 16
Ice VII	3.4	Ref. 17
Platinum	77.8	Ref. 19
MgO	83.2	Calculated at 10 GPa from Ref. 20
Neon	5.7	Calculated at 10 GPa using data from Ref. 26

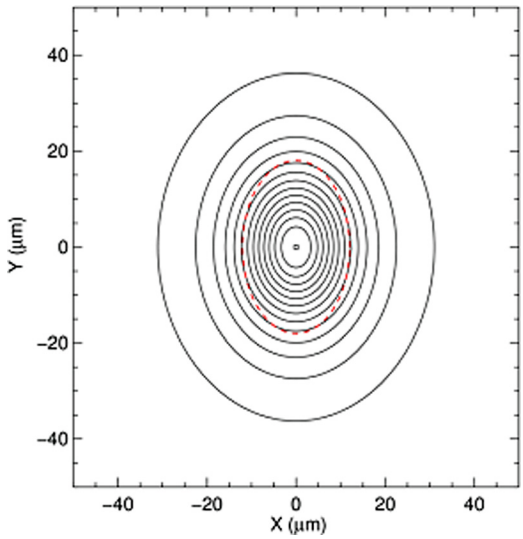

FIG. 4. Temperature contours in the radial plane for a partially absorbing sample heated with an elliptical laser. The contours are 150 K apart, with the peak at 2350 K. The red dashed line shows the FWHM of the elliptical Gaussian laser beam.

B. Anisotropic thermal conductivity

While many samples are polycrystalline and randomly oriented and have isotropic heat flow properties, it is possible to use the laser-heated diamond anvil cell to measure anisotropy in thermal conductivity of oriented single crystals. To demonstrate the ability of our model to simulate 3-D thermal conduction, we modeled laser heating of oriented single-crystal graphite in the LHDAC. An example hotspot is shown in Fig. 6. The thermal conductivity of graphite is highly anisotropic, with the thermal conduction parallel to the graphite sheets being around 220 times faster than thermal conduction along the *c*-axis perpendicular to the sheets.[16] Using the thermal diffusivities from Kato *et al.*,[16] the thermal conductivity values in the directions parallel and perpendicular to the graphite sheets are approximately 1500 W/m K and 6.8 W/m K, respectively. We assumed a

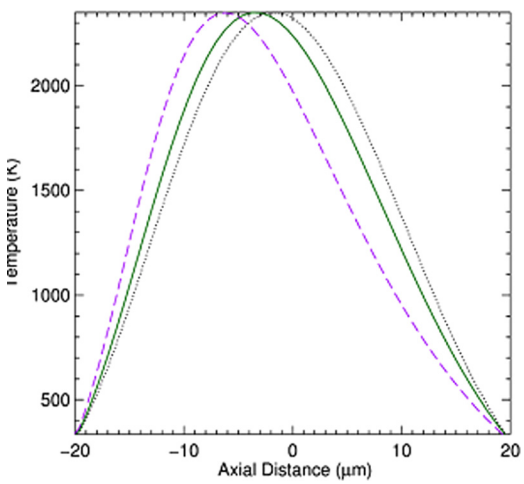

FIG. 5. Axial temperature profiles for partially absorbing samples with optical thickness $\tau = 0.5$ (black dotted line), $\tau = 1.0$ (green solid line), and $\tau = 2.0$ (purple dashed line).

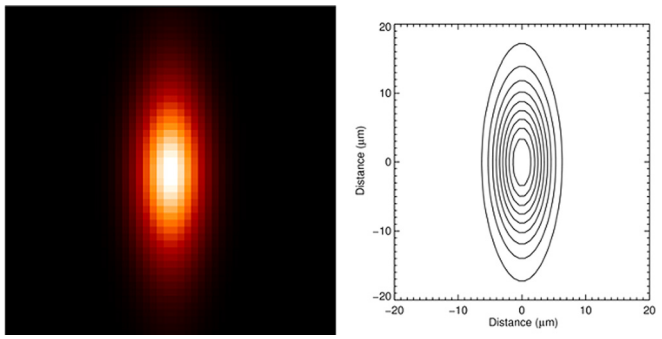

FIG. 6. Modeled hotspot for laser-heated oriented graphite in a DAC. The image on the left shows the modeled intensity at 700 nm wavelength of the 2D hotspot in the radial plane at the surface of the heated graphite. The plot on the right shows intensity contours for the same hotspot.

graphite crystal of thickness 80 μm and radius 60 μm, oriented such that the fast and slow thermal conductivity directions both lay in the radial plane. The insulating material was assumed to be H_2O at ~3 GPa (Ice VII), which has an ambient-temperature thermal conductivity of around 3.4 W/m K.[17] A circular Gaussian laser with a FWHM of 27 μm was used, and the thermal conductivities of all materials other than graphite (diamond anvils, rhenium gasket, and H_2O insulating material) were assumed to be isotropic, so that any ellipticity in the modeled hotspot would be due to the anisotropy of graphite thermal conductivity alone. The ellipticity of the hotspot shown in Fig. 6 is ~2.5, similar to the measured ellipticities for oriented graphite in the LHDAC.[18] The hotspot intensity was calculated using the modeled temperature distribution at the surface of the graphite and assuming Planck emission at 700 nm wavelength. Only the relative hotspot intensities are compared, so the absolute value of the emissivity of the graphite at 700 nm is unimportant.

C. Single- versus double-sided heating with laser absorber

We modeled several temperature distributions for a 10-μm-thick Pt foil between MgO insulation layers in a DAC. Three simulations were run: (1) double-sided laser heating with the Pt foil placed between symmetric 15-μm-thick MgO layers, (2) single-sided heating with the Pt foil between symmetric 15-μm-thick MgO layers, and (3) double-sided heating with the Pt foil between asymmetric MgO layers, with the MgO ~20 μm thick on one side and ~10 μm thick on the other. The sample chamber was assumed to have a radius of 80 μm, and the Pt foil a radius of 40 μm. The lasers had Gaussian intensity profiles with a full width at half maximum of 20 μm. The thermal conductivity of Pt was taken from Terada *et al.*,[19] and the thermal conductivity of MgO from Tang and Dong.[20] The MgO layers were assumed to be transparent and the Pt was assumed to be opaque such that the laser was absorbed only within elements at the edge of the foil. Temperature profiles from each of the three simulations are shown in Fig. 7. In each case, the laser power was adjusted in order for the peak temperature within the sample chamber to reach 2000 K.

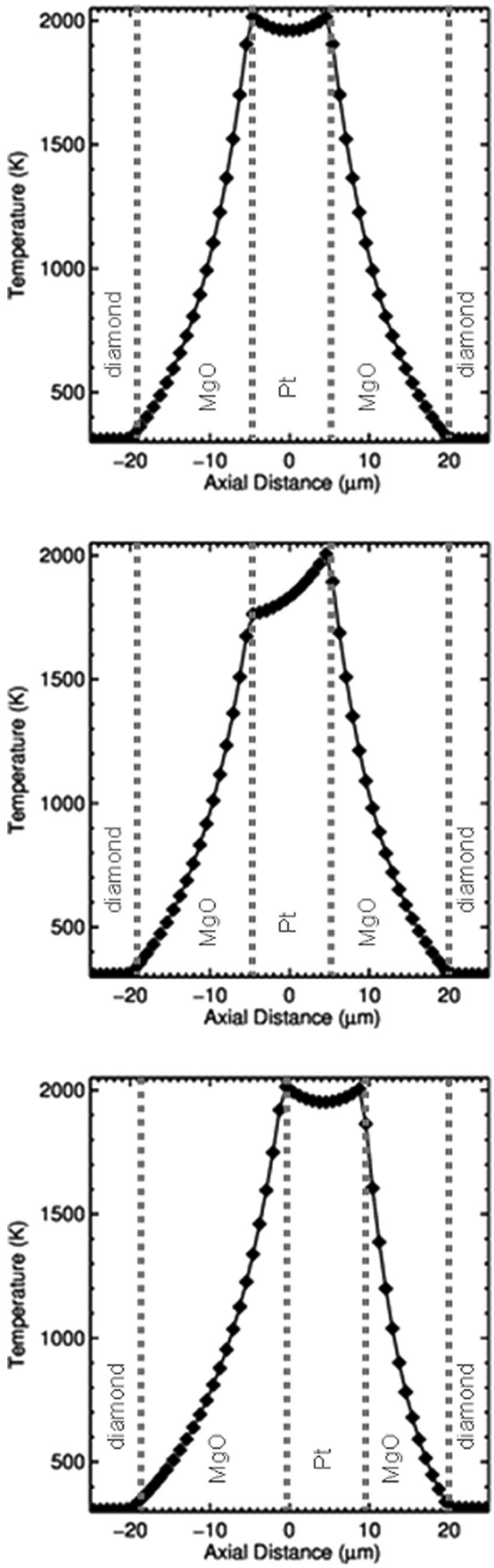

FIG. 7. Modeled axial temperature profiles for a 10-μm-thick Pt foil with MgO insulation layers. The upper plot shows the axial temperature profile through the center of the sample when laser heating is double-sided. The center plot shows the axial temperature profile for single-sided laser heating. The lower plot shows the axial temperature profile for a sample with asymmetric MgO layers and double-sided heating.

In all three simulations, there are steep temperature gradients within the MgO layers relative to the Pt layer. When the heating is double-sided and the insulation layers are symmetric, the central temperatures on each side of the Pt foil are identical. When the laser heats one side only, that side of the foil has a higher peak temperature. For the model parameters used here, the peak temperature is ~12% lower on the unheated side of the Pt foil. The temperature difference between the two sides would be smaller for a thinner foil or a foil with higher thermal conductivity. When the MgO insulation layers are of different thickness, the central temperatures on each side of the foil differ. However, this difference tends to be small, <1% for the model parameters used here. Therefore, measuring the same temperature on each side during double-sided laser heating in a DAC does not mean that the insulation layers are of identical thickness. If the measured temperatures on the two sides differ, it is more likely to be due to differences in laser power or laser absorption than insulation layer thickness.

Another feature of these solutions is that even when symmetric double-sided heating is implemented, the temperature in the middle of the foil is slightly lower than the temperatures at the foil edges. This effect is due to the 3-D nature of heat conduction within the LHDAC, and is not observed in lower-dimensional models. Since a 3D model is needed in order to fully describe temperature gradients within the sample chamber, it is especially important to use a model such as TempDAC when determining the effects of temperature gradients on experimental results. For example, when interpreting measurements of temperature-dependent material properties from X-ray diffraction experiments, it is important to correctly quantify the effect of temperature gradients over the entire 3-D X-ray volume.

D. "Flat-top" laser

One approach to minimizing temperature gradients over the X-ray volume during LHDAC diffraction experiments is to use "flat-top" laser beams [e.g., Refs. 21 and 22]. To create a "flat-top," a beam shaper is used to form a laser intensity distribution that is approximately flat over the extent of the laser spot size. In order to calculate the type of sample temperature gradients that would result in flat-top laser heating experiments, we created a flat-top laser model in TempDAC. It is impossible to create a truly flat laser beam experimentally, so we used an approximately flat-top profile created by summing seven Gaussians. Fig. 8 shows the intensity profile of the modeled flat-top laser beam, which has a FWHM of 21 μm. For comparison, a Gaussian profile with 21-μm FWHM is also shown. Our modeled flat-top laser profile is similar to the experimentally created flat-top beam profile shown by Prakapenka *et al.*[22]

We used TempDAC to model temperature distributions for the flat-top and Gaussian laser profiles shown in Fig. 8. For each laser profile two models were run, one for a partially absorbing olivine sample of thickness 40 μm with single-sided laser heating, and one for a 20-μm-thick Pt foil with symmetric 15-μm-thick MgO insulating layers and double-sided laser heating. In each case, the sample chamber radius

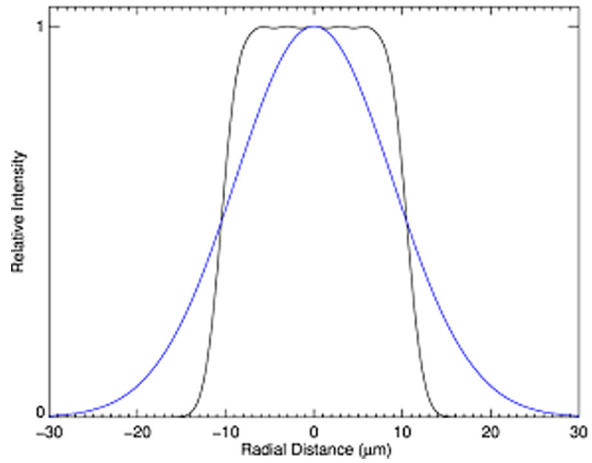

FIG. 8. Comparison of an approximately flat-top laser profile (black line) and Gaussian laser profile (blue line) with the same FWHM of 21 μm.

was 80 μm, and the radius of the Pt foil in the second model was 40 μm. For each laser profile, the total laser power was tuned to result in the same peak temperature in order to more easily compare the temperature distributions. The modeled radial and axial temperature profiles are shown in Figs. 9 and 10. These temperature profiles illustrate several important points. First, a flat-top laser profile does not result in a uniform temperature distribution. Heat must be conducted away from the center of the sample, resulting in non-zero temperature gradients even in areas where the laser profile is very close to flat. Second, the temperature profiles resulting from a flat-top laser are not flatter than the temperature profiles from a Gaussian laser of the same FWHM. In fact, the reverse is true: radial temperature gradients are shallower for the Gaussian laser in both cases. Axial temperature gradients are nearly identical for both laser shapes for the partially absorbing sample [Fig. 9], and shallower for the Gaussian laser within the metal foil [Fig. 10]. This occurs because the Gaussian laser beam deposits proportionally more energy away from the center of the sample, allowing for shallower temperature gradients near the center. Note, however, that because of this the Gaussian laser profile also required more energy in order for the sample to reach the same peak temperature as the flat-top laser (for the model parameters used here, ~12% more absorbed power was required for the metal foil, and ~46% more for the partially absorbing sample). It should also be noted that for a small X-ray volume and a relatively wide laser profile, axial temperature gradients can be more significant than radial temperature gradients. For example, if an X-ray beam ~5 μm in diameter were used with the sample modeled here, the temperature variations within the X-ray spot in the Pt foil would be ~1% in the radial direction and ~12% in the axial direction for the flat-top laser. The axial temperature gradient within the Pt foil would be smaller in the case of a thinner foil or a foil with higher thermal conductivity.

E. Pressure-dependence of hotspot width

As a sample is pressurized, the heat flow environment in the diamond cell becomes more extreme due to the thinning of the insulation layers and the sample. Additional changes in the heat flow may occur because of pressure-induced changes in thermal conductivity and absorption of laser power.[23] Here, we examine how the hotspot size and shape vary at high pressure when the only pressure-induced effect is quasi-hydrostatic thinning of the sample chamber. We performed calculations for a laser-absorbing foil within an insulating medium assuming that all deformation was confined to the thinning of the insulation layers. This approximation is appropriate for an incompressible metal foil within a soft insulation material. We chose a Pt foil (bulk modulus 260 GPa) within Ne insulation layers (bulk modulus ~1 GPa), using an ambient-temperature thermal conductivity for Ne of 5.7 W/m K, appropriate for solid Ne at 10 GPa as calculated using the Leibfried-Schlomann equation[25] and using low-temperature measurements from Weston and Daniels.[26] We also assumed that the sample chamber did not change radius as it thinned. A change in the sample chamber radius would have only a minor effect on the temperature distribution as long as the sample chamber remained wider than the laser beam, since in typical experiments where the laser spot is smaller than the sample chamber the temperature drops to near-ambient well within the sample chamber radius. Our models show that as the sample thins, the peak temperature reached for the same laser power is lower.

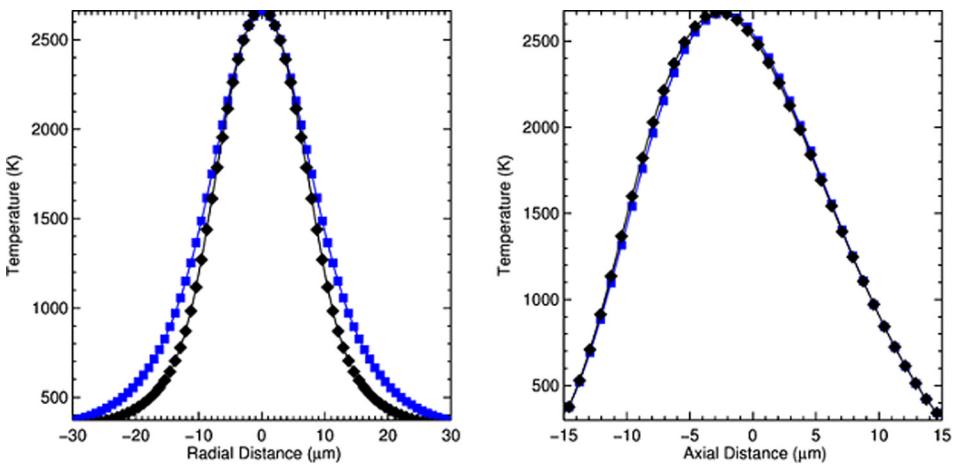

FIG. 9. The plot on the left shows modeled radial temperature profiles through the center of a partially absorbing olivine sample with an optical thickness of 1.0 for the flat-top (black line and symbols) and Gaussian (blue line and symbols) laser beams shown in Fig. 8. The plot on the right shows the corresponding axial temperature profiles through the center of the sample.

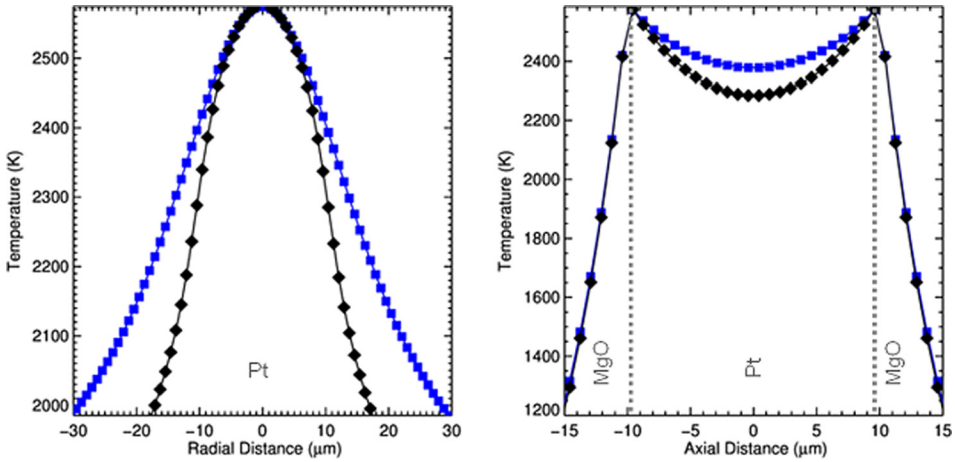

FIG. 10. The plot on the left shows calculated radial temperature profiles at the surface of a Pt foil for the flat-top (black line and symbols) and Gaussian (blue line and symbols) laser beams shown in Fig. 8. The plot on the right shows the corresponding axial temperature profiles through the center of the sample.

Fig. 11 shows the calculated peak temperature as a function of insulation layer thickness for a Pt foil in a Ne medium, heated on each side with a Gaussian laser having a FWHM of 20 μm and 3.5 W output power. For every $\sim$2 μm thinning, the peak temperature drops $\sim$100 K. This effect is solely due to pressure-induced sample thinning, but a similar effect would be observed for a pressure-induced increase in thermal conductivity (we ignored the pressure increase in thermal conductivity for these simulations). Therefore, care must be taken when interpreting changes in temperature vs. power curves taken at different pressures. We also modeled cases for which the laser power is increased in order to reach the same peak temperature with a thinner sample. Fig. 12 shows radial temperature profiles for models with insulation layers that are 20 μm, 16 μm, and 12 μm thick on each side. In order to reach the same temperature of 2260 K, the sample for which the insulation layers had thinned to 16 μm required 10% more power; for 12-μm insulation layers, 25% more laser power was required. As Fig. 12 shows, when the sample thins at higher pressure, the radial temperature profile becomes narrower. The effects of thinned insulation layers on temperatures and hotspot shapes have also been observed in models and measurements by Panero and Jeanloz[24] and Kavner and Panero.[2] Note that the narrowing of the radial temperature profile at higher pressure is due primarily to the change in geometry rather than a pressure-induced change in thermal conductivity. Our calculations show that if the thermal conductivity of a sample is increased without changing the sample thickness, the shape of the hotspot at a particular peak temperature does not change (although more laser power is needed to reach the same peak temperature). For a particular sample and laser geometry and peak temperature, the temperature gradient is independent of the absolute value of the sample thermal conductivity (although the temperature-dependence of thermal conductivity does matter).

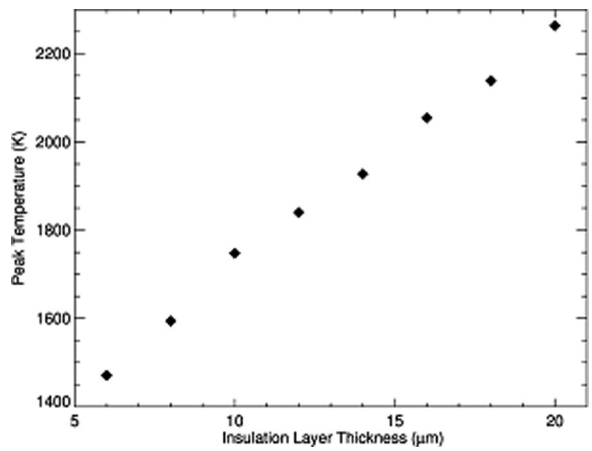

FIG. 11. Peak temperature for constant laser power as a function of single-sided insulation layer thickness for an incompressible Pt foil heated within a soft Ne insulating medium in the LHDAC. Slight deviations from a smooth curve are due to the resolution limits of the mesh used in the numerical model.

V. CONCLUSIONS

We have created and validated a full 3-D numerical model, TempDAC, for calculating temperature distributions within the LHDAC applicable to steady-state continuous heating experiments. Several interesting properties of LHDAC temperature distributions are illustrated by our example calculations. Temperature gradients will exist in both the axial and radial directions, with the particulars of the temperature gradients depending on the experimental geometry and the sample thermal conductivity. The

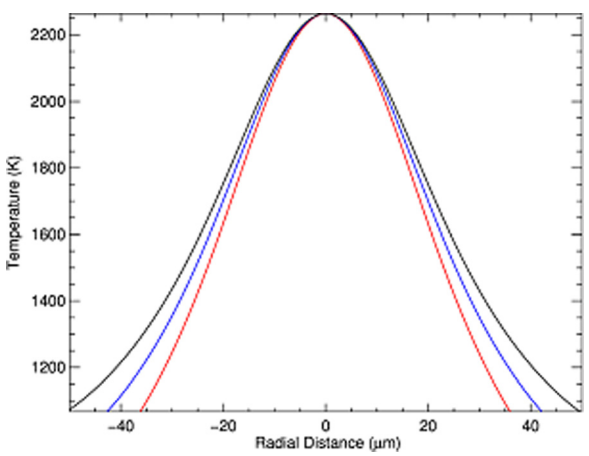

FIG. 12. Radial temperature profile at the surface of an incompressible Pt foil heated within a soft Ne medium as a function of single-sided thickness of the symmetric insulation layers: 20 μm (black line), 16 μm (blue line), and 12 μm (red line).

temperature distribution is strongly dependent on the experimental geometry, with the sample thickness and the particular shape of the laser beam intensity profile both having significant influences on the resulting temperature gradients. The extreme temperature gradients that form within the sample during laser heating are three-dimensional, and the 3D nature of the heat conduction must be taken into account when making predictions regarding LHDAC temperature gradients and when interpreting X-ray diffraction data that have been obtained during laser heating.

The results of our models for some special cases of sample physical properties and sample and heating laser geometry suggest ways to enhance the design of high-pressure, high-temperature laser heating experiments. For example, our models support the idea of measuring hotspot ellipticity as an indicator of anisotropy in heat flow properties; however, these experiments must be accompanied by models in order to interpret results. Elliptical laser beams and anisotropic thermal conductivity both result in elongated hotspots, but the ellipticity of the hotspots is less than that of the laser beam or the anisotropy of thermal conductivity due to axial heat flow. The models also help guide priorities for sample loading and experimental setup. Contrary to conventional wisdom, our models show that asymmetrically thick insulation layers do not necessarily result in significant differences in peak temperatures on each side of a heated foil. Moreover, a "flat-top" laser beam, while it can produce a shallow temperature gradient near the center of the sample if the laser spot size is large enough, does not produce a temperature gradient that is flatter or more uniform than would be produced by a Gaussian beam profile of similar width.

Our model and the results presented here can be useful tools in designing LHDAC experiments and interpreting LHDAC temperature measurements. Our code will be made freely available to anyone within the community who wishes to use it.

ACKNOWLEDGMENTS

This work was supported by NSF EAR-0969033.

[1]R. Boehler, Rev. Geophys. **38**(2), 221–245, doi:10.1029/1998RG000053 (2000).
[2]A. Kavner and W. R. Panero, Phys. Earth Planet. Inter. **143–144**, 527–539 (2004).
[3]M. Manga and R. Jeanloz, J. Geophys. Res. **102**(B2), 2999–3008, doi:10.1029/96JB02696 (1997).
[4]Z. Konopkova, P. Lazor, A. F. Goncharov, and V. V. Struzhkin, High Press. Res. **31**(1), 228–236 (2011).
[5]K. D. Leinenweber, J. A. Tyburczy, T. G. Sharp, E. Soignard, T. Diedrich, W. B. Petuskey, Y. Wang, and J. L. Mosenfelder, Am. Mineral. **97**, 353–368 (2012).
[6]S. Bodea and R. Jeanloz, J. Appl. Phys. **65**(12), 4688–4692 (1989).
[7]B. Kiefer and T. S. Duffy, J. Appl. Phys. **97**, 114902 (2005).
[8]X. Li, M. Manga, J. H. Nguyen, and R. Jeanloz, Geophys. Res. Lett. **23**(25), 3775–3778, doi:10.1029/96GL03648 (1996).
[9]W. R. Panero and R. Jeanloz, J. Geophys. Res. **106**(B4), 6493–6498, doi:10.1029/2000JB900423 (2001).
[10]D. L. Heinz and R. Jeanloz, in *High-Pressure Research in Mineral Physics*, edited by M. H. Manghnani and Y. Syono (American Geophysical Union, Washington DC, 1987), p. 113–127.
[11]M. Manga and R. Jeanloz, in *Properties of Earth and Planetary Materials*, edited by M. H. Manghnani and T. Yagi, (American Geophysical Union, Washington DC, 1998), p. 17–25.
[12]J. Hernlund, K. Leinenweber, D. Locke, and J. A. Tyburczy, Am. Mineral. **91**, 295–305 (2006).
[13]Y. Xu, T. J. Shankland, S. Linhardt, D. C. Rubie, F. Langenhorst, and K. Klasinski, Phys. Earth Planet. Inter. **143–144**, 321–336 (2004).
[14]L. Wei, P. K. Kuo, R. L. Thomas, T. R. Anthony, and W. F. Banholzer, Phys. Rev. Lett. **70**(24), 3764–3767 (1993).
[15]R. W. Powell, R. P. Tye, and M. J. Woodman, J. Less-Common Met. **5**(1), 49–56 (1963).
[16]H. Kato, T. Baba, and M. Okaji, Meas. Sci. Technol. **12**, 2074 (2001).
[17]B. Chen, W.-P. Hsieh, D. G. Cahill, D. R. Trinkle, and J. Li, Phys. Rev. B **83**, 132301 (2011).
[18]A. Kavner and C. Nugent, Rev. Sci. Instrum. **79**, 024902 (2008).
[19]Y. Terada, K. Ohkubo, and T. Mohri, Platinum Met. Rev. **49**(1), 21–26 (2005).
[20]X. Tang and J. J. Dong, Proc. Natl. Acad. Sci. U.S.A. **107**(10), 4539–4543 (2010).
[21]G. Shen, H.-K. Mao, and R. J. Hemley, in *Advanced Materials'96—New Trends in High Pressure Research: Proceedings of the 3rd NRIM ISAM* (Tsukuba, Japan, 1996), pp. 149–152.
[22]V. B. Prakapenka, A. Kubo, A. Kuznetsov, A. Laskin, O. Shkurikhin, P. Dera, M. L. Rivers, and S. R. Sutton, High Press. Res. **28**(3), 225–235 (2008).
[23]E. S. G. Rainey and A. Kavner, "Thermal conductivity of (Mg,Fe)SiO_3 perovskite measured at high pressure and high temperature," J. Geophys. Res. (unpublished).
[24]W. R. Panero and R. Jeanloz, Rev. Sci. Instrum. **72**(2), 1306 (2001).
[25]M. Roufosse and P. G. Klemens, Phys. Rev. B **7**, 5379 (1973).
[26]H. T. Weston and W. B. Daniels, Phys. Rev. B **29**, 2709 (1984).